

https://dspace.org/

Aberration-induced vortex splitting in amplified orbital angular momentum beams

Harrison, Justin; Buono, Wagner Tavares; Forbes, Andrew; Naidoo, Darryl

2023

https://hdl.handle.net/10539/49548

Harrison, J., Buono, W. T., Forbes, A., & Naidoo, D. "Aberration-induced vortex splitting in amplified orbital angular momentum beams," Opt. Express 31, 17593-17608 (2023)

Downloaded from a DSpace repository. https://dspace.org/

Research Article | Vol. 31, No. 11 / 22 May 2023 / Optics Express 17593
Optics EXPRESS

Aberration-induced vortex splitting in amplified orbital angular momentum beams

JUSTIN HARRISON,[1,2,*] WAGNER TAVARES BUONO,[2,3] ANDREW FORBES,[2] AND DARRYL NAIDOO[1,2]

[1] CSIR National Laser Center, P.O. Box 395, Pretoria 0001, South Africa
[2] School of Physics, University of the Witwatersrand, Johannesburg, Wits 2050, South Africa
[3] Center for Nano Science and Technology, Fondazione Istituto Italiano di Tecnologia, Milano, Italy
[*] jharrison@csir.co.za

Abstract: Here we report the generation and power amplification of higher-order ($l = 2$) orbital angular momentum (OAM) beams using a compact end-pumped Nd:YAG Master-Oscillator-Power-Amplifier (MOPA) design. We analysed the thermally-induced wavefront aberrations of the Nd:YAG crystal using a Shack-Hartmann sensor as well as modal decomposition of the field and show that the natural astigmatism in such systems results in the splitting of vortex phase singularities. Finally, we show how this can be ameliorated in the far field through engineering of the Gouy phase, realising an amplified vortex purity of 94% while achieving an amplification enhancement of up to 1200%. Our comprehensive theoretical and experimental investigation will be of value to communities pursuing high-power applications of structured light, from communications to materials processing.

© 2023 Optica Publishing Group under the terms of the Optica Open Access Publishing Agreement

1. Introduction

Light beams carrying orbital angular momentum (OAM) - commonly referred to as twisted or vortex beams - are characterized by a quantized angular momentum of $l\hbar$ per photon with an azimuthally (ϕ) varying phase structure $\exp(il\phi)$, where l represents the topological charge or number of twists in the optical wavefront per unit wavelength, and have been extensively reviewed to date [1,2]. One common form of OAM beams are described mathematically by the Laguerre-Gauss eigenmodes, LG_p^l, where l and p are azimuthal and radial indices, respectively (see theory later). The annular intensity profile and twisting helical wavefront of pure $\mathrm{LG}_0^{l=1}$ beams have been utilised in various applications, such as optical particle trapping and manipulation [3,4], material processing [5], free-space optical communications [6], super-resolution microscopy [7] and image processing [8]. However, LG_0^l beams of $l>1$ promise to increase the bandwidth of free-space [9] and quantum optical communication [10] and offer greater flexibility for enhanced material ablation applications [11]. In practice, especially in manufacturing applications, average powers exceeding 20 W are required while maintaining the modal purity of the LG_0^l beams.

OAM beams are easy to create and can be generated internal (intra-) or external (extra-) to the laser cavity. Intra-cavity generation has a long history and has been extensively reviewed to date [12–15], with recent advances including an interferometric mode transforming output coupler [16], astigmatic mode converters [17–19], optical parametric oscillators (OPO) [20–22], annular pumping [23–25] and exploiting spherical aberration [26–28]. Extra-cavity generation of OAM beams is likewise very well established [29–31] and typically involves the transformation of a laser with a Gaussian LG_0^0 output using elements that impart an azimuthally varying phase, generally fabricated for a specific topological charge output. Further, such phase-only approaches (that impart an azimuthally varying phase to the input Gaussian beam) do not produce true LG_0^l modes; instead, they are hypergeometric modes [32] which manifest in the Laguerre-Gaussian basis as many unwanted radial modes [33]. Recent advances to overcome this include amplitude and phase control using geometric phase metasurfaces [34–36], while OAM charge tuneability

#487616 https://doi.org/10.1364/OE.487616
Journal © 2023 Received 14 Feb 2023; revised 8 Mar 2023; accepted 10 Mar 2023; published 10 May 2023

Optics EXPRESS

can be achieved by dynamic computer generated holograms [37] written to digital micro-mirror devices (DMDs) [38] or spatial light modulators (SLMs) [30].

Most of these approaches have been demonstrated only at low power, a limitation that can be overcome by performing power-scaling using one or more master oscillator power amplification (MOPA) modules. A MOPA module consists of a laser gain medium (slab, cylindrical rod, thin-disk or fibre geometries) which is optically excited using an external pump source, typically a narrow-wavelength diode-laser, in either an end- or side-pumping configuration - depending on the choice of the gain medium. Side-pumped configurations offer high amplification potential but require a minimum threshold input seed power to amplify efficiently and are subjected to high-intensity pump radiation, which increases the risk of thermally-induced phase aberrations [39,40]. In end-pumped systems, the seed beam is co-axially propagated with the pump beam for efficient spatial overlap with the gain region and provides a cost-effective, controllable and robust solution for low to intermediate amplification. Power scaling of OAM beams using end-pumped MOPAs has been reported in stressed Yb fibres [41], Ho:YAG crystal rods [42], Er-doped ring core fibres [43] and Nd:YVO_4 crystal rods [44]. In general, both the delivery of the pump light as well as its localization to a small area result in both thermal and non-thermal aberrations [45], distorting the desired mode. To date, the impact of this on OAM purity and power scaling ability has not been reported.

In this work, we investigate the generation and power amplification by a compact end-pumped Nd:YAG MOPA system, with the aim to produce higher-order and high purity OAM modes. We reveal that higher-order Laguerre-Gaussian (LG_0^2) beams result in vortex splitting, which we study both theoretically and experimentally with the aid of a Shack-Hartmann wavefront sensor and modal decomposition. We show that vertical astigmatism, leading to a Gouy phase anomaly, is introduced to the system via a pump beam distortion which is caused by the inherent design of compact end-pumped MOPA systems. Additionally, we show experimentally and computationally that the physical separation of the phase singularities can be reversed in the far field by exploiting the Gouy phase shift. Using these findings we are able to report an amplified vortex purity of up to 94% while achieving an amplification enhancement of up to 1200%.

2. Theory

2.1. Laguerre-Gaussian and Hermite-Gaussian modes

The modes to be discussed in this paper include OAM-carrying Laguerre-Gaussian beams, and non-OAM-carrying Hermite-Gaussian modes. Laguerre-Gaussian modes are a subset of circularly symmetric solutions of the paraxial wave equation, written in cylindrical coordinates (ρ, ϕ, z) as

$$\begin{aligned} \mathrm{LG}_p^l(\rho,\phi,z) = \frac{1}{\omega(z)}\sqrt{\frac{2p!}{\pi\,(|l|+p)!}}\left(\frac{\sqrt{2}\rho}{\omega(z)}\right)^{|l|}\mathrm{L}_p^l\left[2\left(\frac{\rho}{\omega(z)}\right)^2\right] \\ \exp\left[-\left(\frac{\rho}{\omega(z)}\right)^2\right]\exp\left[i\xi_l^p(z)\right]\exp\left[-\frac{ik\rho^2}{2R(z)}\right]\exp\left[-il\phi\right] \end{aligned} \tag{1}$$

Where l & p are the azimuthal and radial integers of the L_p^l generalized Laguerre polynomial, which quantify the topological charge and number of bright rings, respectively, k, ω_0, $\omega(z)$ and $R(z)$ are the wavenumber, beam waist, beam size at position z and wavefront curvature. The parameter $\xi_l^p(z) = (2p + |l| + 1)\arctan(z/z_R)$ is known as the Gouy phase. Hermite Gaussian (HG) modes are also solutions to the paraxial wave equation and are expressed in cartesian coordinates

Optics EXPRESS

(x, y, z):

$$\mathrm{HG}_{n,m}(x,y,z) = \frac{1}{\omega_0}\sqrt{\frac{2}{2^{n+m}\pi\, n!\, m!}}H_n\left(\frac{\sqrt{2}}{\omega_0}\,x\right)H_m\left(\frac{\sqrt{2}}{\omega_0}\,y\right) \exp\left[-\frac{x^2+y^2}{\omega_0^2}\right]\exp\left[i\xi_{n,m}(z)\right]\exp\left[-\frac{ik(x^2+y^2)}{2R(z)}\right] \tag{2}$$

Where k and $R(z)$ are the wavenumber and wavefront curvature, respectively, and H_j is the Hermite polynomial of order j and ω_0 is the beam waist radius of the fundamental $\mathrm{HG}_{0,0}$ mode, subsequent higher order $\mathrm{HG}_{n,m}$ modes scale in beam size according to their indices by factors of $\sqrt{1+2n}$ and $\sqrt{1+2m}$ in the x and y-directions, respectively. Similarly to LG modes, HG modes also form a complete basis set of orthogonal eigenfunctions and can be used to decompose any square-integrable function. Similarly, $\xi_{n,m}(z) = (n+m+1)\arctan(z/z_R)$ is known as the Gouy phase.

2.2. Wavefront aberrations

In an amplifier system, it is important not only to increase the amplitude of the input mode but to preserve its profile, both in amplitude and phase, however, we know that these systems involve energy transfer between pump photons and the crystal lattice ions. Only a portion of absorbed photons can potentially contribute towards amplification, the remaining fraction is converted to heat, defined as the quantum defect heating coefficient (η_h = 0.24-0.3 for 0.5% atm. Nd:YAG). The build-up of heat in the crystal medium changes the refractive index experienced by the input mode and causes aberrations in the wavefront $W_\mathrm{ab}(x, y)$ of the amplified beam, commonly referred to as thermally-induced aberrations. A tool often used for characterizing wavefront aberrations is the Zernike Polynomials.

The Zernike polynomials and weighting coefficients can be obtained using a Shack-Hartmann wavefront sensor (SHWF) by measuring a probe beam, typically a Gaussian mode, after interaction with the aberrations, in this case, the end-pumped Nd:YAG crystal. The aberrated wavefront can be numerically reconstructed in the Zernike polynomial basis, for simplicity expressed using the singe-index (j) representation, as follows [46]:

$$W_\mathrm{ab}(x,y) = W_\mathrm{ref}(x,y) - \sum_{j=0}^{N} C_j Z_j(x,y) \tag{3}$$

Where C_j are the Zernike coefficients (units of waves) for the corresponding j_th Zernike polynomial $Z_j(x, y)$. From this point onward, the single-index (j) Zernike polynomial and weighting coefficient are replaced by the traditional double-index (l, n) representation (i.e. $\{Z_j, C_j\} \rightarrow \{Z_n^l, C_n^l\}$) according to the OSA/ANSI standard. To decouple the aberrations induced by the optical system from those caused by the end-pumped Nd:YAG crystal, a reference wavefront $W_\mathrm{ref}(x, y)$ measurement with the pump beam turned off is subtracted from the wavefront measurement when the pump beam is turned on, thus isolating the thermally-induced aberrations $W_\mathrm{ab}(x, y)$ of the end-pumped Nd:YAG crystal only. The wavefront $W_\mathrm{ab}(x, y)$ (in units of waves) can then be easily converted to a transmittance function $t_\mathrm{ab}(x, y)$

$$t_\mathrm{ab}(x,y) = e^{i\,2\pi\,W_\mathrm{ab}(x,y)} \tag{4}$$

Any LG_p^l mode can then be modulated by the phase aberration $t_\mathrm{ab}(x, y)$ to create an aberrated optical field $\Psi(x, y)$

$$\Psi(x,y) = \mathrm{LG}_p^l \times t_\mathrm{ab}(x,y) \tag{5}$$

The procedure of measuring real wavefront aberrations in optical systems and subsequent numerical phase reconstruction is a useful tool for performing computational simulations to better understand and characterize complex optical processes.

Optics EXPRESS

2.3. Modal Decomposition

An elegant approach to characterize the effects of wavefront aberrations on the purity of any arbitrary optical field $\Psi(x, y)$ is to perform modal decomposition, which describes modes that constitute $\Psi(x, y)$ using a complete orthogonal basis set, such as the circularly symmetric Laguerre-Gaussian or the rectangular symmetric Hermite-Gaussian modes [47]. When the field $\Psi(x, y)$ lacks circular symmetry, the rectangular symmetric Hermite-Gaussian $\mathrm{HG}_{n,m}$ modes are used as the modal decomposition expansion basis set. We can expand $\Psi(x, y)$ into constituent $\mathrm{HG}_{n,m}$ modes as follows:

$$\begin{aligned}\Psi(x, y) &= \sum_{m=0}^{\infty}\sum_{n=0}^{\infty} a_{n,m}\mathrm{HG}_{n,m}(x, y) \\ &= \sum_{m=0}^{\infty}\sum_{n=0}^{\infty} |a_{n,m}|e^{i\phi_{n,m}}\mathrm{HG}_{n,m}(x, y)\end{aligned} \tag{6}$$

Where $a_{n,m}$ are complex-amplitude terms containing the modal weightings $|a_{n,m}|$ and complex modal phases $\phi_{n,m} = \arg(a_{n,m})$. The complex-amplitude coefficient $a_{n,m}$ can be determined by taking the inner product of the $\mathrm{HG}_{n,m}$ modes with the aberrated field $\Psi(x, y)$:

$$a_{n,m} = \iint_{-\infty}^{\infty} \mathrm{HG}^{*}_{n,m}\Psi(x, y)\mathrm{d}x\mathrm{d}y \tag{7}$$

With a sufficiently large set of amplitude coefficients $|a_{n,m}|$ and corresponding phases $\phi_{n,m}$, the aberrated field $\Psi(x, y)$ is reconstructed using Eq. (6). The amplitude weightings should be normalized so that $\sum_{n,m} |a_{n,m}|^2 = 1$.

2.4. Gouy Phase in astigmatic systems

In astigmatic systems, the lack of circular symmetry is a strong motivation for using $\mathrm{HG}_{n,m}$ modes instead of LG^{l}_{p} modes. There are mainly two ways of characterising an astigmatic mode: to analyse the coordinates and its parameters separately [48] or to use a modal decomposition of the beam including the aberrated wavefront. The Gouy phase plays an important role in both cases. In the first, the difference in Rayleigh ranges for x/y coordinates creates a phase difference between the constituent Hermite polynomials of the mode. In the latter, the Gouy phase is responsible for an intramodal phase proportional to the mode order accumulated over propagation. This intra-modal phase can be responsible for local constructive/destructive interference, which can describe simple effects such as the focusing caused by a lens [49] and even complex phenomena like self-imaging [50]. Moreover, the latter will be used to explain the vortex-splitting effect observed. Naturally, the astigmatic wavefront and its lack of circular symmetry will introduce an asymmetry in the modal decomposition. On the HG basis, this translates to modes of some indices being preferred over others, where the indices are associated with a specific coordinate. Since the level of detail in the wavefront increases, more modes will be seen in the decomposition and the different mode orders create propagation effects.

3. Experimental setup

The experimental setup, depicted in Fig. 1, consisted of three main parts; part *a*) was the spatial light modulator (SLM) beam shaping system used to select LG^{2}_{0} modes, part *b*) the end-pumped MOPA system, and part *c*) the aberration measurement using a Shack-Hartmann wavefront sensor.

Part *a*): A Gaussian beam LG^{0}_{0} at wavelength 1064 nm with a continuous-wave output power of 8 W was collimated and projected onto a water-cooled SLM (Pluto-2) phase-only screen with a

Optics EXPRESS

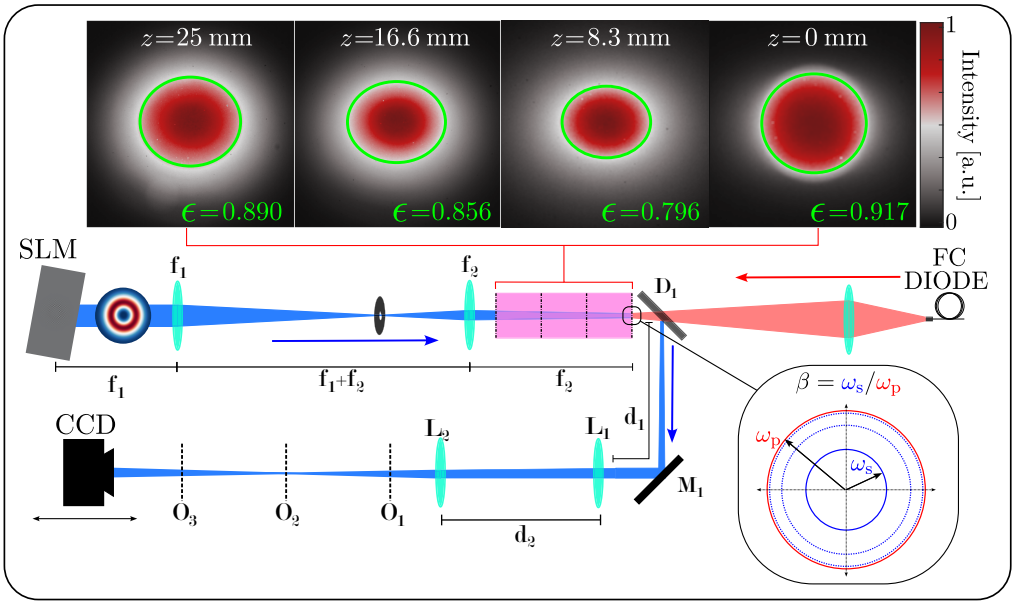


Fig. 1. Schematic diagram showing the experimental layout with figure insets (top) showing the pump intensity profile (not to scale) measured at various z-positions of the Nd:YAG crystal (pink) with (green) ellipticity values (ϵ). The circled figure inset (bottom right), schematically depicts the cross-section of the fixed pump ω_p (red circle) and varying seed ω_s (blue circles) beam sizes at the pumped face of the crystal (z = 0 mm).

D4σ radius of ω_0 = 3 mm. Computer-generated holograms (CGH) of the LG_0^2 modes of varying sizes were displayed on the SLM screen to perform complex-amplitude phase modulation. The reflected LG_0^2 beams were spatially filtered using a 4f imaging system with a variable aperture at 2F from the SLM screen to remove the undesired diffraction orders. An afocal 5× demagnifying lens pair of focal lengths f_1 = 500 mm & f_2 = 100 mm was used to relay image the LG_0^2 beams to the pumped end of an Nd:YAG crystal rod. The LG_0^2 beam waist sizes encoded on the CGH were made large to maximize the area on the SLM screen and spatial overlap with the Gaussian envelope to extract maximal power, without exceeding the damage threshold of the liquid-on-crystal layer (200 W/cm^2).

Part *b*): The MOPA system was constructed using an Nd:YAG crystal (0.5% atm. ϕ4 mm x 25mm) mounted in a water-cooled (18 C°) copper block and the pump source was an 808 nm, 200 μm core diameter multi-mode fibre-coupled (FC) diode laser module P_p = 0 – 60 W. The exit face of the diode laser fibre tip was single-lens imaged (1:2) to the surface of the crystal through a 45° dichroic mirror D_1, which is high-reflective coated at 1064 nm wavelength and anti-reflective coated at 808 nm wavelength, to a achieve a FWHM radius of ω_p = 200 μm. The pump beam size ω_p was kept constant throughout the experiment. At the image plane of the pumped crystal face (z = 0 mm), we considered LG_0^2 beam sizes with 4σ radii of ω_s = 100 μm, 160 μm and 200 μm, corresponding to $\beta = \omega_s/\omega_p$ values of 0.5, 0.8 and 1, respectively, as illustrated by the concentric rings in the bottom right inset of Fig. 1. Since the plane of the SLM screen is relay imaged to the crystal face, only the CGH phase profiles were changed to select different LG_0^2 beam sizes to make the setup consistent, repeatable and simple to switch between β values without any realignment required. The output beams were propagated over a distance d_1 = 430 mm from the pumped end of the crystal to lens a L_1 = 250 mm, with lens L_2 = 37.5 mm placed at the beam waist position $d_2 = Z_0$ of lens L_1. The beam was analysed symmetrically

Optics EXPRESS

through the focus of L_2 using a CCD camera mounted on a motorized translation stage for each β value at pump powers of P_p = 25 W, 40 W and 60 W. The translation stage was adjusted slightly for each measurement so that the focus of L_2 was at position O_2, with $O_1 = O_2 - 25$ mm & $O_3 = O_2 + 25$ mm being the forward and backward limits of the motorized stage.

Part *c*): A CGH displayed was on the SLM screen to select a Gaussian beam with a D4σ beam radius of ω_g = 1.33 mm and the 4F imaging lenses were changed to $f_1 = f_2$ = 300 mm for 1:1 imaging to the crystal face, so that the Gaussian beam was approximately 3× larger than ω_p, to probe a large area of the thermally induced aberration. The pixel area of the SHWS was filled using lenses L_1 = 150 mm and L_2 = 400 mm to expand the aberrated Gaussian probe by 2.6×. The SHWS was placed at the image plane of L_2 and wavefront aberrations $W_{ab}(x, y)$ were then recorded at pump at powers of P_p = 25 W, 40 W and 60 W.

4. Results/discussion

4.1. Pump beam distortion

Efficient coupling of the pump light into the crystal rod is crucial for obtaining a high amplification factor while keeping the thermally-induced aberrations to a minimum. In general, for end-pumped systems specifically, the exit face of the fibre tip is focused through a 45° dichroic mirror to the face of the crystal. We assume that the pump beam remains spatially circular and uniform during this process. However, as shown by the top row inset in Fig. 1, when measured experimentally we find that the pump beam profile is asymmetric and its degree of asymmetry varies across the crystal length. This asymmetry is measured in terms of ellipticity ϵ, which indicates the ratio of the minor (short) axis to the major (long) axis second-moment beam width. When the value of ϵ is equal to 1, the beam profile is perfectly circular. At the image plane of the fibre, located at z = 0 mm, the measured ellipticity value was ϵ = 0.917. This value decreased to ϵ = 0.796 at z = 8.3 mm and gradually became more circular as the beam propagated further along the crystal and reached ϵ = 0.890 at z = 25 mm. Using a ray optic simulator, the converging pump beam passing through a 45° dichroic mirror (fused quarts $n \sim 1.45$) was modelled, shown in Fig. 2. We see that the outer edges of the light rays marked A and B, have different incident angles $\alpha_A \neq \alpha_B$ normal to the mirror surface and therefore will refract at different rates. When $\alpha_A = \alpha_B$, the outer rays will converge at the same point, but since this is no longer the case the focal point of the rays along the x-axis of the beam shift laterally. The rays along the y-axis remain unaffected since they have equal incident angles $\alpha_A = \alpha_B$ to the surface of the mirror. The density of the light rays is also not uniformly distributed after passing through the dichroic mirror and is skewed toward side A which has the smallest angle normal to the mirror.

4.2. Analysing the thermal aberrations

Due to quantum defect heating effects from energy transfer between the pump photons and crystal, the asymmetric spatial profile after passing through the 45° dichroic mirror manifests in the heat distribution inside the crystal, resulting in non-circular thermally-induced aberrations. A Shack-Hartmann wavefront sensor (SHWS) was used to measure the Zernike coefficients of the induced wavefront aberrations at pump powers of P_p = 25 W, 40 W and 60 W, shown in Fig. 3.

As expected for a typical end-pumped amplifier, the circularly symmetric negative defocus C_2^0 and positive primary spherical C_4^0 Zernike coefficients were obtained, which scaled proportionately with increasing P_p. Pertinent to this paper is the strong appearance of non-circular primary C_2^2 and secondary C_4^2 vertical astigmatism coefficients, caused by the elliptical heat load created by the distorted pump beam along the horizontal direction and also scaled proportionately with P_p. In comparison, the primary C_2^{-2} and secondary C_4^{-2} oblique astigmatism coefficients were not significant and did not show a clear relationship with P_p. The combination of defocus C_2^0 and vertical astigmatism C_2^2 and C_4^2 aberrations create a cylindrical lens effect, resulting in the

Optics EXPRESS

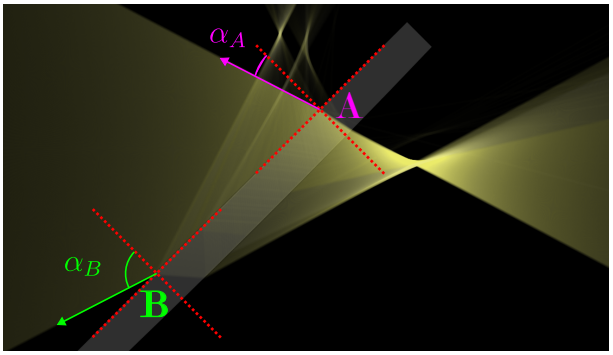


Fig. 2. Ray Optics Simulation depicting the difference in the incident angles (α_A & α_B) between the outer rays (points A & B) of the pump beam (yellow) normal to the dichroic mirror (grey), resulting in a distorted pump beam at the focal plane.

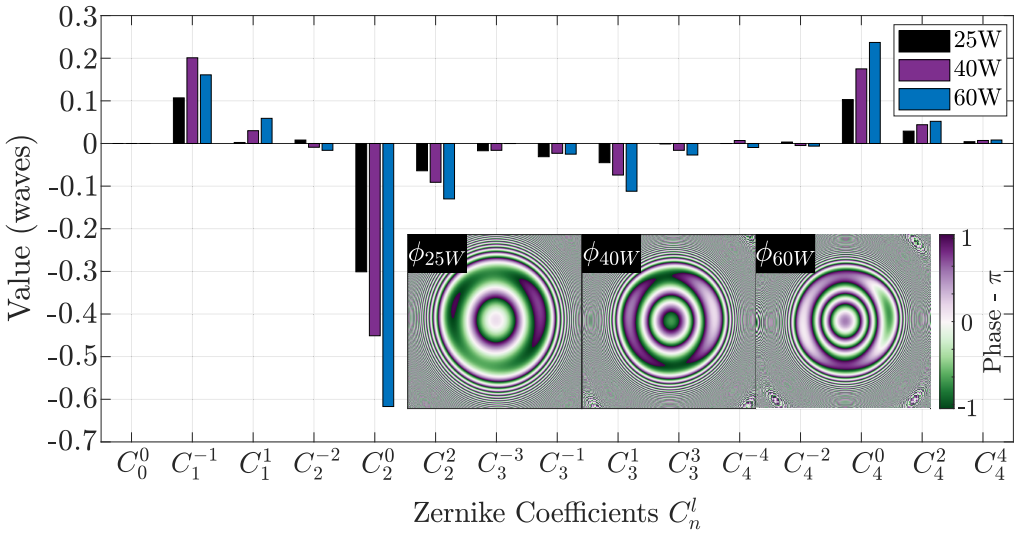


Fig. 3. A bar plot showing the Zernike coefficients C_n^l of the thermally-induced wavefront aberrations for incident pump powers P_p of 25 W (black), 40 W (purple) and 60 W (blue), respectively. The figure inset shows the corresponding reconstructed phase profiles of the wavefront aberration for the pump powers ϕ_{P_p}.

$yz-$ and $xz-$ optical axes experiencing different focusing conditions. Interestingly, we see that horizontal coma coefficient C_3^1 scaled proportionality with P_p and was more prevalent than vertical C_3^{-1} coma, which remained constant. The dependence of P_p on the horizontal coma coefficient correlates well with the inhomogeneous distribution of refracted pump rays, shown in Fig. 2, leading to a non-uniform lens in the horizontal direction. There is, however no inclination in the vertical direction, and thus, no distortion occurs. This figure illustrates how astigmatism can arise from a single effectively transparent element without any measurable curvature. For the measured Zernike coefficients, based on the prevalence, weighting and scaling behaviour with input pump power it is clear that the intensity distribution of the pump distortion through the 45° mirror has translated directly to the thermal aberrations of the crystal in the form of strong vertical C_2^2 and C_4^2, and horizontal coma C_3^1 coefficients.

Optics EXPRESS

Using the measured Zernike coefficients, it is easy to numerically recreate the phase profile of the thermal aberration using the wavefront reconstruction process, as explained by Eqs. (3), (4) and (5). The reconstructed phase profiles $\phi_{25\,\mathrm{W}}$, $\phi_{40\,\mathrm{W}}$ and $\phi_{60\,\mathrm{W}}$, excluding tip C_1^{-1} and tilt C_1^1 coefficients, are shown as insets in Fig. 3.

4.3. How did this affect the OAM beams

The degree of spatial overlap β between seed and pump sizes is an important parameter to consider when constructing end-pumped MOPA systems. Higher values of β overlap better with the gain region and can extract more power but become more susceptible, especially at high pump powers, to distortions due to non-uniform spatial interactions with the thermal aberrations, whereas smaller values of β extract less power but are less susceptible to aberrations. Therefore, to find the optimal overlap for higher-order OAM modes specifically, we considered a range of β = 0.5, 0.8 and 1. The phase interaction between the LG_0^2 beams and the thermally-induced wavefront aberration was performed using low input seed powers of $P_\mathrm{s} \sim 10$ mW. This was done so that no additional power-dumping optical components were required after the MOPA stage which could potentially introduce secondary aberrations. Nevertheless, since the gain of an amplifier only modulates the intensity of the mode, the phase interaction will have the same effect - regardless of the seed power.

In the top row of Fig. 4, we show experimental results of the low-power LG_0^2 beams with different β values after passing through the MOPA system at P_p = 60 W, and propagating through the lens system described in Fig. 1 and recorded at positions O_1, O_2 & O_3. We see that the intensity profiles of the aberrated LG_0^2 beams before (O_1) and after (O_3) the focus positions have two distinct valleys which became more apparent as β increased. The observed effect is the well-known "vortex splitting" phenomenon and is indicative of vortex beams perturbed by astigmatic aberrations, typically caused by tilted or cylindrical lenses. However, to our knowledge, this is the first time the effect has been reported in compact end-pumped amplifiers due to thermal distortions. Interestingly, perturbed symmetry of the modes appeared to recover to a symmetrical state at the focus position O_2 regardless of β.

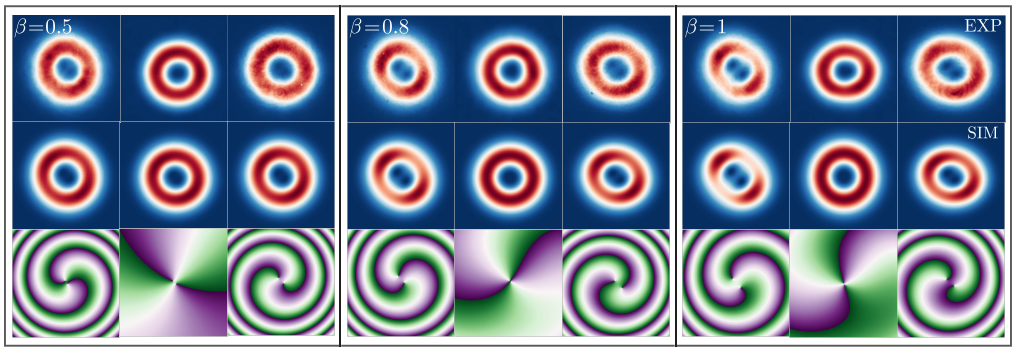


Fig. 4. Experimental results (top row) of the LG_0^2 OAM modes with β = 0.5 (left grid), 0.8 (middle grid) and 1 (right grid) after interaction with the thermally-induced pump P_p = 60 W aberration, measured at positions O_1 (left column), O_2 (middle column) and O_3 (right column) with corresponding simulated results of the beam intensities (middle row) and phases (bottom row).

To analyse this effect more closely, the experiment was simulated using Eq. (1) to generate LG_0^2 modes and modulated by the reconstructed phase aberration $\phi_{60\,\mathrm{W}}$ at the plane of the pumped crystal and propagated through the optical system d_1, L_1, d_2 and L_2 and recorded at positions O_1, O_2 and O_3. The simulated intensities, middle row of Fig. 4, showed excellent agreement with

Optics EXPRESS

the experimental data across all values of β and also indicate a recovery in the symmetry of the modes at O_2. The phase profiles of the split simulated data, bottom row Fig. 4, show the physical separation of the phase singularities at locations O_3 & O_1 appear to merge at O_2.

4.4. Analyzing the splitting using Gamma

To track the phase singularities between positions O_1 and O_3, a local minima search algorithm was used to identify the grid locations (x, y) of the zero-intensity valleys - corresponding to the location of the phase singularities, as shown by the insets of Fig. 5, for the simulated data. Visually inspecting Fig. 4, the distance between the phase singularities, defined as d_{sep}, increases with an increase in β. However, when measuring d_{sep} of the top and middle rows we found that d_{sep} was larger at positions O_1 and O_3 for $\beta = 0.5$ than it was for $\beta = 1$. This is because the beam divergence is different for each β; thus, d_{sep} by itself is not very useful and can not be used to directly compare the magnitude of splitting in terms of β.

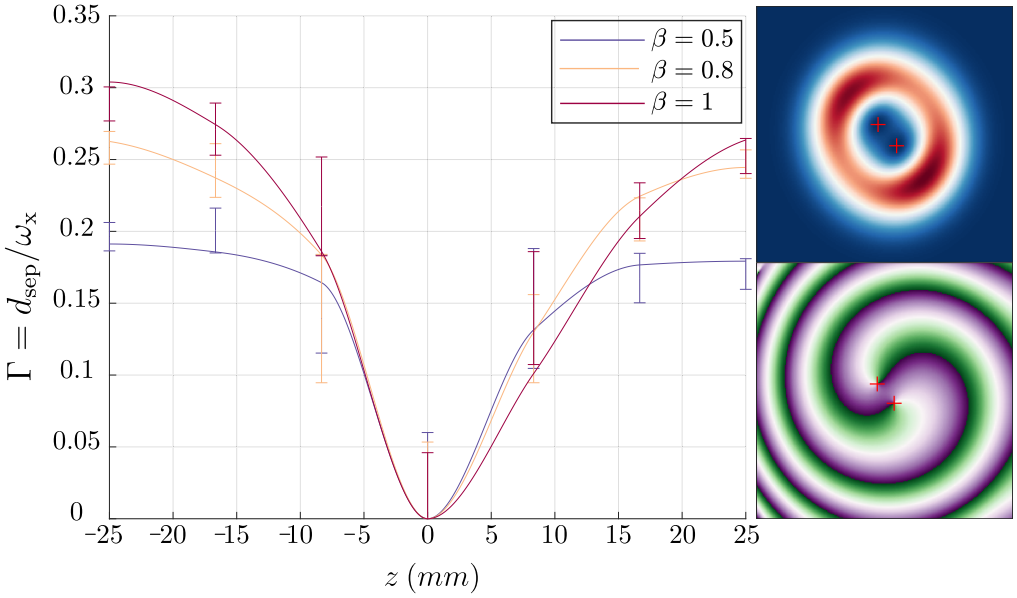


Fig. 5. Graph showing the simulated (solid lines) behaviour of Γ through the focus of lens L_2 for $\beta = 0.5$ (purple), 0.8 (yellow) and 1 (red), with experimentally measured Γ values plotted as error bars. An example (right) of the algorithm used to locate (red crosses) the intensity minima (top) with correlation to the phase singularities (bottom) used to calculate d_{sep}.

For a more general description of OAM separation, we define a unit-less variable Γ, which is the ratio of d_{sep} and the beam diameter ω_x that quantifies the "degree of OAM separation" as a relative value that accounts for the beam size. Γ visually quantifies the distortion so that when $d_{\text{sep}} \longrightarrow 0$ then $\Gamma = 0$ and the beam spatially resembles a symmetric LG_0^2 mode, and when $d_{\text{sep}} \neq 0$ the separation of phase singularities become more apparent and Γ>0. With this definition of Γ, d_{sep} and ω_x were measured experimentally and in the simulation at evenly spaced points between O_1 to O_3 for the different values of β - plotted in Fig. 5. The solid lines indicate Γ curves for the simulated data, and the error bars are experimentally measured data points which show good agreement. The trajectory of the initially separated phase singularities at O_1 converge at the focus position O_2 and separate from then on to a slightly lower value of Γ at O_3- which is also visually apparent in Fig. 4. Additionally, the gamma values at positions O_1 and O_3 for the

Optics EXPRESS

different values of β corroborate well with the visual degree of OAM separation that we observed in Fig. 4.

4.5. Modal content

The value Γ provides a good quantitative description of the visual degree of spatial distortion but does not provide information regarding the modal purity of the aberrated LG_0^2 beam. To investigate the modal purity, a computational modal decomposition is performed on the modes aberrated by $\phi_{60\,\mathrm{W}}$ at the position of L_1 for values of $\beta = 0.5, 0.6, 0.7, 0.8, 0.9$ and 1, following the procedure of Eq. (5) and (6). Since the radial symmetry of the LG_0^2 beam has been broken due to the separation of the phase singularities, the modal decomposition was performed in the rectangular symmetric $HG_{n,m}$ basis of Eq. (2). For reference, an unaberrated or 100% pure LG_0^2 beam is described in the $HG_{n,m}$ basis as a superposition of three $HG_{n,m}$ modes:

$$LG_0^{\pm 2} = \sqrt{0.5}HG_{1,1} + \sqrt{0.25}HG_{0,2} + \sqrt{0.25}e^{[\pm i\pi/2]}HG_{2,0}$$

The computational modal decomposition results are depicted by the bar chart of Fig. 6 (top), showing the modal power weightings of each mode in the $HG_{n,m}$ basis for the different values of β. The insets in Fig. 6 (top) show the intensity profiles of each β for which modal decomposition was performed and Fig. 6 (bottom) below shows the evolution of the dominant modal weightings. We see that for $\beta = 0.5$, the purity of the LG_0^2 mode remained high at 94% and decreased gradually as β increased, such that for $\beta = 1$ the modal purity decreased to 82%. It is clear that the purity of the LG_0^2, defined by its three constituent modes $HG_{1,1}$, $HG_{2,0}$ and $HG_{0,2}$, is affected by the selection of β. In the modal traces of Fig. 6 (bottom), we see that the $HG_{2,0}$ and $HG_{0,2}$ do not decrease at the same rate with β, which is most likely due to the horizontal symmetry of the $HG_{2,0}$ mode coupling more strongly with the aberrations induced by the horizontally distorted pump beam. The combination of defocus C_2^0 and vertical astigmatism C_2^2 and C_4^2 aberrations create a cylindrical lens effect, resulting in the $yz-$ and $xz-$ optical axes experiencing different focusing conditions and can explain the reason for enhanced coupling of the horizontally structured $HG_{n,m}$ modes. Additionally, the appearance of the horizontally structured $HG_{2,1}$ and $HG_{3,0}$ modes are significantly larger than the vertically structured $HG_{1,2}$ and $HG_{0,3}$ modes. Based on the $\{n, m\}$ indices and power weightings of the new modes appearing as β increases, it suggests that the LG_0^2 mode is being converted to mostly LG_0^3 and a small portion of LG_0^1.

In Fig. 5 and 6, we have been able to quantify the spatial distortion and modal purity of the aberrated LG_0^2 beams as a function of β for a high pump power of $P_\mathrm{p} = 60$ W. Based on the modal weightings of Fig. 6, we know that the LG_0^2 beam is no longer a pure mode after the amplifier. However, we have yet to interpret the apparent phase singularity recombination at position O_2, $\Gamma \longrightarrow 0$, which spatially resembles a pure LG_0^2 mode. We then performed a computational modal decomposition in the $HG_{n,m}$ basis on the $\beta = 1$, $\phi_{60\,\mathrm{W}}$ aberrated LG_0^2 beam at positions O_1 and O_2 where the beams have Γ values of 0.3 and 0, respectively.

Figure 7 (top) shows the results of the decomposition, where the insets depict the intensity and phase of the initially simulated beams (left inset) with the corresponding reconstructed intensity and phase (right inset) for both the near-field (O_1) and far-field (O_2) positions. The modal decomposition was performed in both planes with the constituent modes having their propagation also simulated, accounting for the difference in the size of modes between the two planes. The results are consistent with the fact that modal weightings should not change in free space propagation. Therefore, for them to have the same modal weightings and composition, but different spatial profiles, their relative phases must also be different.

It is important to notice that the constituent modes for a pure LG_0^2 all belong to the same mode order $n + m = 2$. When astigmatism is introduced in this system, modes of different orders $HG_{2,1}$

Optics EXPRESS

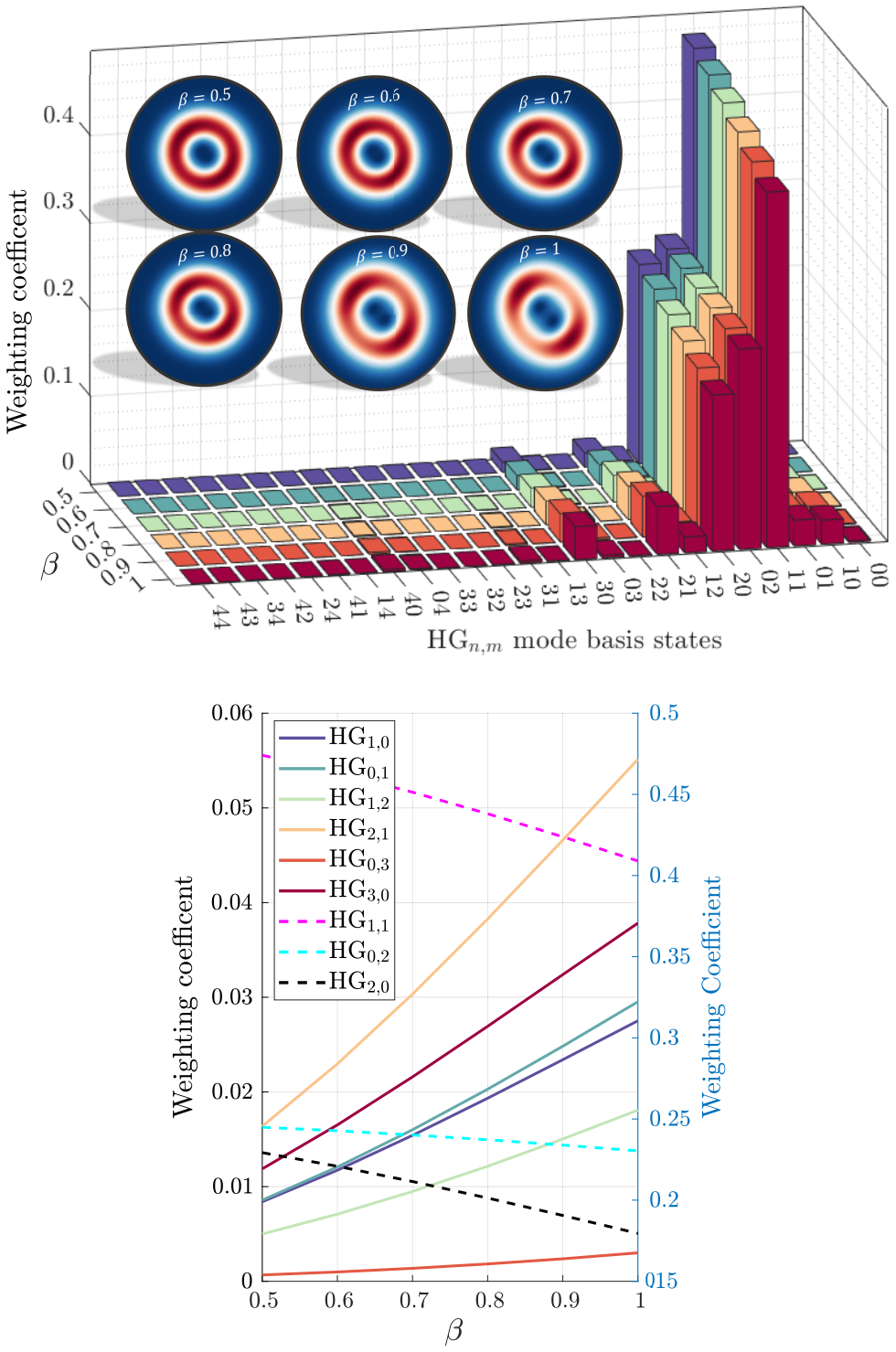


Fig. 6. Computational modal decomposition results (top) in the HG$_{n,m}$ basis of LG$_0^2$ modes for β = 0.5, 0.6, 0.7, 0.8, 0.9, 1 aberrated by phase $\phi_{60\,\mathrm{W}}$, with insets showing the corresponding split OAM spatial profiles. (bottom) Traces of the main constituent HG$_{n,m}$ modes in the bar plot increase (solid lines left axis) and decrease (dashed lines right axis) as a function of β.

Optics EXPRESS

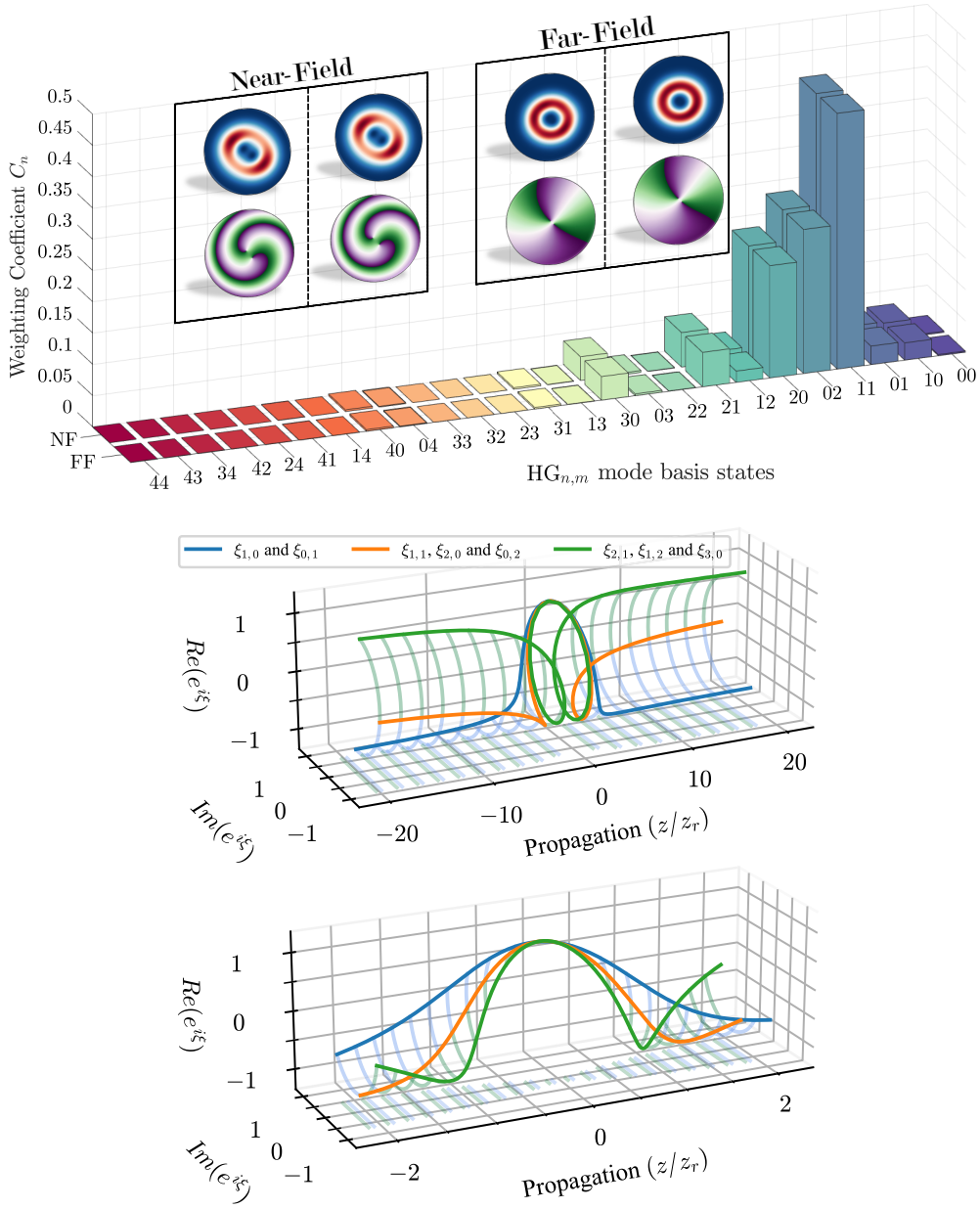


Fig. 7. Differences in Near-Field and Far-Field. In the top figure insets, we see the transverse intensity and phase profiles of the simulated and reconstructed aberrated beam, alongside their modal weightings. The middle and bottom plots show the evolution of the Gouy phase of the three different mode orders that possess relevant weightings. Blue(green) lines connecting blue(green) and orange lines show the difference between the phases, and the light blue(green) lines on the bottom are the length of each corresponding line showing the module of the difference between the phases.

and $HG_{3,0}$ (order $n + m = 3$)) become more relevant, as seen on Fig. 7. For this reason, we recall the importance of the Gouy phase in modal content with order diversity, highlighted in recent works [48,50,51].

Optics EXPRESS

For this argument, the initial phases between modes of the same order are not relevant, only the phase accumulated in propagation between near and far fields. Effectively, the Gouy phase $\xi(z)$ makes it so that each order of modes gains a phase in propagation proportional to its order and the function arctan of the propagation distance. In the limit of $z \to \pm\infty$, it reaches the asymptotic values of π, $3\pi/2$ and 2π for orders 1, 2 and 3, respectively. This means that, over propagation from near to far field, modes of order 1 and 3 will gain a phase of $\pm\pi/2$ relative to modes of order 2. Those accumulated intramodal phases create a dynamic behaviour where the field, composed of paraxial modes which are invariant to propagation, can change in propagation. The Gouy phases are illustrated in Fig. 7, middle and bottom rows, only for orders 1, 2 and 3 for simplicity. When $z \to 0$ the phase differences, depicted as blue (green) arches and projections on the bottom, drop sharply to zero. On regions far from the origin, the relative phase differences reach the asymptotic value of $\pm\pi/2$. The consequence of this relative phase difference is the observation of an intensity pattern that changes on propagation and, in this case, the observation of vortex splitting happening in the near field but not in the far field.

4.6. Amplification results

Due to the sensitivity of the d_{sep} measurement and for consistency between β values, the Gaussian beam size and power on the SLM, and all subsequent optical components were kept fixed thought the experiment - only the CGHs were swapped. This meant that the reflected power of the SLM varied for each β value due to the reduced spatial overlap with the Gaussian envelope during complex-amplitude shaping, resulting in maximum LG_0^2 mode powers of $P_{\text{s}} = 90$ mW, 215 mW and 300 mW, for $\beta = 0.5$, 0.8 and 1, respectively. The variations in maximum power did not deter from the thermally-induced aberration study since the measurements were performed at fixed low-powers ~10 mW. However, rather than reduce the power of all the beams to $P_{\text{s}} = 90$ mW, we performed amplification using the maximum output for each value of β. We have already shown that by exploiting the Gouy phase shift, the symmetry of the aberrated higher-order OAM beam can be recovered at the far field, therefore, for an application such as material processing where the spatial profile at the focus is more important than the modal purity, a high value of β - corresponding to a higher amplified output power is desirable. If modal purity is required, a low β can be selected and amplified. Nevertheless, the power density of the Gaussian envelope is already at the damage threshold of the SLM device and therefore the current generated seed powers can not be increased further. Therefore, the amplification results for each value of β should be considered as an independent, rather than a comparative amplification study of LG_0^2 modes. The amplification results for $\beta = 0.5$, 0.8 and 1, are shown in Fig. 8 as a function of the input pump power. For $\beta = 0.5$, the input seed power grew from 90 mW to 1.1 W, $\beta = 0.8$ grew from 215 mW at the input to 2.15 W, and $\beta = 1$ grew from 300 mW to 2.6 W, corresponding to gain factors of 12×, 10× and 8.6×, respectively. For comparison of the amplifier performance, the amplified output powers curves of the LG_0^2 modes are compared to that of the fundamental Gaussian mode LG_0^0 for $\beta = 0.5$, 0.8 and 1, created on the SLM using complex-amplitude shaping, with matching input powers of 90 mW, 215 mW and 300 mW, respectively. The LG_0^0 modes achieved maximum output powers of 1.17 W, 2.3 W and 2.8 W, corresponding to gain factors of 13×, 10.7× and 9.3× over the LG_0^2 modes for $\beta = 0.5$, 0.8 and 1, respectively. The slight advantage in the gain factor of the Gaussian mode is due to its high central peak intensity which has a better overlap with the intensity of the pump beam in the crystal volume, compared to the lower peak intensity LG_0^2 beam profile with a zero intensity central region. An exponential function was fit to all data points, confirming that the amplification is well within the small-signal gain region, where exponential growth is expected. In Fig. 8, the intensity of the LG_0^2 and LG_0^0 modes are presented on the right of the amplification curve plot, measured at position O_1, for a maximum pump power of $P_{\text{p}} = 60$ W. We can observe that the OAM splitting is evident during power scaling, and this splitting has the same dependence on the choice of β. The insets

Optics EXPRESS

displaying the fundamental mode outputs include the beam ellipticity ϵ measurement in green. We can see that β is directly proportional to the ellipticity, which decreases from $\epsilon = 0.9$ for $\beta = 0.5$ to $\epsilon = 0.81$ for $\beta = 1$. This observation reveals that compact end-pumped MOPAs does not adversely affect the amplified output quality of the fundamental mode, resulting in only minor ellipticity, and thus, the thermally-induced aberrations are usually ignored. However, we demonstrate here that the higher-order OAM modes, subjected to the same thermal aberration, are considerably more susceptible to these aberrations and require a lower value of β than the fundamental modes.

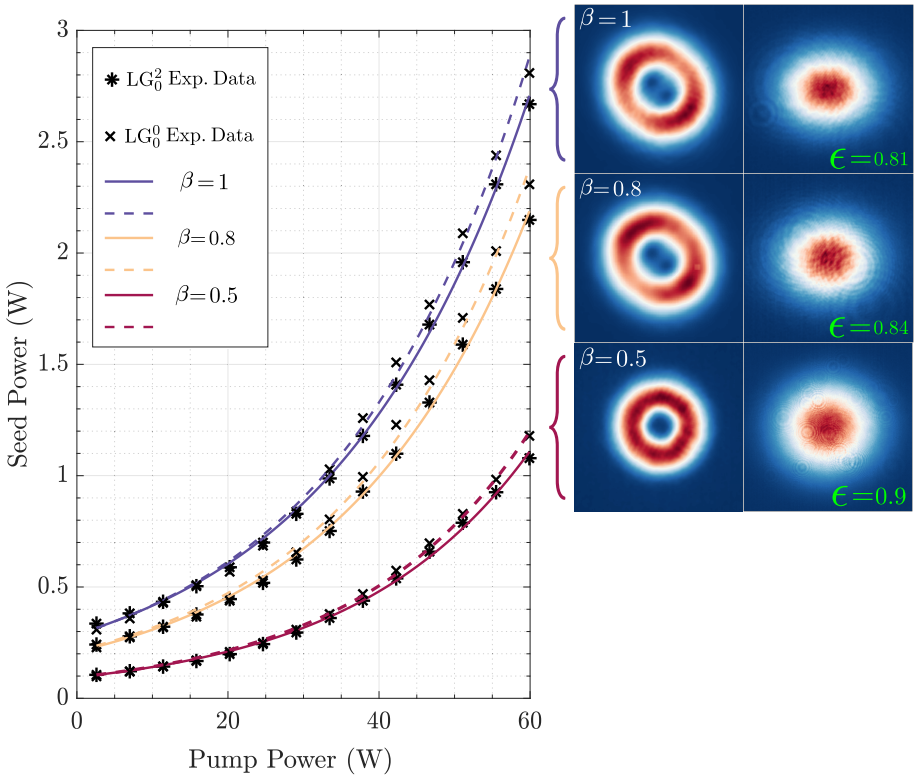


Fig. 8. The output powers of the LG$_0^2$ higher-order OAM modes (marked with black asterisks) and a comparison with the fundamental Gaussian LG$_0^0$ mode (marked with black crosses) were measured experimentally for β values of 0.5 (red), 0.8 (yellow), and 1 (purple). An exponential fit was applied to the experimental data points for both the LG$_0^2$ (represented by solid lines) and the LG$_0^0$ modes (represented by dashed lines). The right figure insets display the transverse beam intensity profiles at the maximum pump power $P_p = 60$ W for the LG$_0^2$ (left column) and LG^{0}0 (right column) modes for different β values, including the ellipticity values (marked in green) for the LG$_0^0$ outputs.

5. Conclusion

We have shown that compact end-pumped Nd:YAG crystal rod MOPA designs are inherently susceptible to non-circular aberrations due to a horizontal distortion of the pump beam when focusing through a 45° dichroic mirror. We show that the phase-interaction of higher-order OAM beams LG$_0^2$, of varying seed-pump spatial overlap values β, with the produced wavefront aberration results in separation of the phase-singularities and quantified using a new variable Γ.

Optics EXPRESS

Modal decomposition in the $HG_{n,m}$ revealed that the purity of the LG_0^2 modes decreased as β increased - resulting in an increase in the level of distortion Γ. Interestingly, we show that the Gouy phase shift anomaly for astigmatic beams can be exploited so that $\Gamma \rightarrow 0$ in the far-field and spatially recovers to a pure circular OAM mode, for any choice of β. Our results describe the conditions for β in higher-order OAM mode amplification processes to provide a high-spatial and high-modal purity in the far field.

Disclosures. The authors declare that there are no conflicts of interest related to this article.

Data availability. Data underlying the results presented in this paper are not publicly available at this time but may be obtained from the authors upon reasonable request.

References

1. A. Forbes, "Perspectives on the orbital angular momentum of light," J. Opt. **24**(12), 124005 (2022).
2. S. Franke-Arnold, "30 years of orbital angular momentum of light," Nat. Rev. Phys. **4**(6), 361 (2022).
3. M. Padgett and R. Bowman, "Tweezers with a twist," Nat. Photonics **5**(6), 343–348 (2011).
4. H. Zhang, X. Li, H. Ma, M. Tang, H. Li, J. Tang, and Y. Cai, "Grafted optical vortex with controllable orbital angular momentum distribution," Opt. Express **27**(16), 22930 (2019).
5. K. Toyoda, F. Takahashi, S. Takizawa, Y. Tokizane, K. Miyamoto, R. Morita, and T. Omatsu, "Transfer of light helicity to nanostructures," Phys. Rev. Lett. **110**(14), 143603 (2013).
6. X. Yan, L. Guo, M. Cheng, and J. Li, "Controlling abruptly autofocusing vortex beams to mitigate crosstalk and vortex splitting in free-space optical communication," Opt. Express **26**(10), 12605 (2018).
7. T. Watanabe, Y. Iketaki, T. Omatsu, K. Yamamoto, M. Sakai, and M. Fujii, "Two-point-separation in super-resolution fluorescence microscope based on up-conversion fluorescence depletion technique," Opt. Express **11**(24), 3271 (2003).
8. A. Aleksanyan, N. Kravets, and E. Brasselet, "Multiple-Star System Adaptive Vortex Coronagraphy Using a Liquid Crystal Light Valve," Phys. Rev. Lett. **118**(20), 203902 (2017).
9. A. E. Willner, H. Huang, Y. Yan, Y. Ren, N. Ahmed, G. Xie, C. Bao, L. Li, Y. Cao, Z. Zhao, J. Wang, M. P. J. Lavery, M. Tur, S. Ramachandran, A. F. Molisch, N. Ashrafi, and S. Ashrafi, "Optical communications using orbital angular momentum beams," Adv. Opt. Photonics **7**(1), 66 (2015).
10. R. Fickler, G. Campbell, B. Buchler, P. K. Lam, and A. Zeilinger, "Quantum entanglement of angular momentum states with quantum numbers up to 10,010," Proc. Natl. Acad. Sci. U. S. A. **113**(48), 13642–13647 (2016).
11. M. Duocastella and C. B. Arnold, "Bessel and annular beams for materials processing," Laser Photonics Rev. **6**(5), 607–621 (2012).
12. A. Forbes, "Structured light from lasers," Laser Photonics Rev. **13**(11), 1900140 (2019).
13. T. Omatsu, K. Miyamoto, and A. J. Lee, "Wavelength-versatile optical vortex lasers," J. Opt. **19**(12), 123002 (2017).
14. A. Forbes, "Advances in orbital angular momentum lasers," J. Lightwave Technol. **41**(7), 2079–2086 (2023).
15. A. Forbes, "Controlling light's helicity at the source: orbital angular momentum states from lasers," Phil. Trans. R. Soc. A **375**(2087), 20150436 (2017).
16. J. W. T. Geberbauer, W. R. Kerridge-Johns, and M. J. Damzen, ">30 W vortex LG 01 or HG 10 laser using a mode transforming output coupler," Opt. Express **29**(18), 29082 (2021).
17. J. Pan, Y. Shen, Z. Wan, X. Fu, H. Zhang, and Q. Liu, "Index-Tunable Structured-Light Beams from a Laser with an Intracavity Astigmatic Mode Converter," Phys. Rev. Appl. **14**(4), 044048 (2020).
18. N. S. Gottesman, M. L. Lukowski, J. T. Meyer, C. Hessenius, E. M. Wright, and M. Fallahi, "Intra-Cavity Astigmatic Mode Converting VECSEL," IEEE Photonics J. **14**(4), 1–6 (2022).
19. S. Wang, S.-L. Zhang, P. Li, M.-H. Hao, H.-M. Yang, J. Xie, G.-Y. Feng, and S.-H. Zhou, "Generation of wavelength- and OAM-tunable vortex beam at low threshold," Opt. Express **26**(14), 18164 (2018).
20. V. Sharma, S. C. Kumar, A. Aadhi, H. Ye, G. K. Samanta, and M. Ebrahim-Zadeh, "Tunable vector-vortex beam optical parametric oscillator," Sci. Rep. **9**(1), 1–7 (2019).
21. V. Sharma, S. Chaitanya Kumar, G. K. Samanta, and M. Ebrahim-Zadeh, "Tunable, high-power, high-order optical vortex beam generation in the mid-infrared," Opt. Express **30**(2), 1195 (2022).
22. A. Aadhi, V. Sharma, and G. K. Samanta, "High-power, continuous-wave, tunable mid-IR, higher-order vortex beam optical parametric oscillator," Opt. Lett. **43**(10), 2312 (2018).
23. T. H. Kim, J. S. Park, J. W. Kim, D. J. Kim, and E. J. Park, "Direct Generation of a Laguerre-Gaussian-Mode Optical Vortex Beam in a Single-Frequency Nd:YVO4 Unidirectional Ring Laser," J. Korean Phys. Soc. **75**(8), 557–560 (2019).
24. J. Li, Y. Yao, J. Yu, K. Xia, and C. Zhou, "Efficient Vortex Laser With Annular Pumping Formed by Circle Dammann Grating," IEEE Photonics Technol. Lett. **28**(4), 473–476 (2016).
25. Y. Yang, Y. Li, C. Wang, and C. Yang, "Research on 946 nm LG 01 mode laser considering thermal effect," Laser Phys. **32**(9), 095801 (2022).
26. S. P. Chard, P. C. Shardlow, and M. J. Damzen, "High-power non-astigmatic TEM00 and vortex mode generation in a compact bounce laser design," Appl. Phys. B: Lasers Opt. **97**(2), 275–280 (2009).

Optics EXPRESS

27. M. Wang, Y. Ma, Q. Sheng, X. He, J. Liu, W. Shi, J. Yao, and T. Omatsu, "Laguerre-Gaussian beam generation via enhanced intracavity spherical aberration," Opt. Express **29**(17), 27783 (2021).
28. Q. Sheng, A. Wang, Y. Ma, S. Wang, M. Wang, Z. Shi, J. Liu, S. Fu, W. Shi, J. Yao, and T. Omatsu, "Intracavity spherical aberration for selective generation of single-transverse-mode Laguerre-Gaussian output with order up to 95," PhotoniX **3**(1), 4 (2022).
29. A. Forbes, M. de Oliveira, and M. R. Dennis, "Structured light," Nat. Photonics **15**(4), 253–262 (2021).
30. A. Forbes, A. Dudley, and M. McLaren, "Creation and detection of optical modes with spatial light modulators," Adv. Opt. Photonics **8**(2), 200–227 (2016).
31. C. Rosales-Guzmán, B. Ndagano, and A. Forbes, "A review of complex vector light fields and their applications," J. Opt. **20**(12), 123001 (2018).
32. E. Karimi, G. Zito, B. Piccirillo, L. Marrucci, and E. Santamato, "Hypergeometric-gaussian modes," Opt. Lett. **32**(21), 3053–3055 (2007).
33. B. Sephton, A. Dudley, and A. Forbes, "Revealing the radial modes in vortex beams," Appl. Opt. **55**(28), 7830 (2016).
34. M. de Oliveira, M. Piccardo, S. Eslami, V. Aglieri, A. Toma, and A. Ambrosio, "Radially and azimuthally pure vortex beams from phase-amplitude metasurfaces," arXiv, arXiv:2205.15890 (2022).
35. M. Jin, B. Sanchez-Padilla, X. Liu, Y. Tang, Z. Hu, K. Li, D. Coursault, G. Li, and E. Brasselet, "Spin-orbit modal optical vortex beam shaping from dielectric metasurfaces," Adv. Opt. Mater. **2022**, 2202149 (2022).
36. D. Coursault and E. Brasselet, "Nanostructured silica spin–orbit optics for modal vortex beam shaping," Nanophotonics **11**(4), 805–812 (2022).
37. J. Pinnell, V. Rodríguez-Fajardo, and A. Forbes, "Probing the limits of orbital angular momentum generation and detection with spatial light modulators," J. Opt. **23**(1), 015602 (2021).
38. S. Scholes, R. Kara, J. Pinnell, V. Rodríguez-Fajardo, and A. Forbes, "Structured light with digital micromirror devices: a guide to best practice," Opt. Eng. **59**(04), 1 (2019).
39. Y. Yu, J. Di, W. Qu, and A. Asundi, "Measurement of thermal effects of diode-pumped solid-state laser by using digital holography," Appl. Opt. **57**(19), 5385 (2018).
40. X. Zhang, X. Zhang, and A. Xiang, "Analysis of thermal effect and beam wavefront properties for LD-pumped Q-switch Nd:YAG laser," Opt. Laser Technol. **49**, 268–273 (2013).
41. M. Koyama, T. Hirose, M. Okida, K. Miyamoto, and T. Omatsu, "Nanosecond vortex laser pulses with millijoule pulse energies from a Yb-doped double-clad fiber power amplifier," Opt. Express **19**(15), 14420 (2011).
42. Y. Li, Z. Zhang, J. K. Miller, and E. Johnson, "Ho:YAG rod amplifier for vortex beams," *2015 IEEE Photonics Conf.*, IPC 2015 3, 321–322 (2015).
43. Q. Kang, P. Gregg, Y. Jung, E. L. Lim, S.-U. Alam, S. Ramachandran, and D. J. Richardson, "Amplification of 12 OAM Modes in an air-core erbium doped fiber," Opt. Express **23**(22), 28341 (2015).
44. S. H. N. S. H. Noh, D. J. K. D. J. Kim, and J. W. K. J. W. Kim, "High power generation of adaptive laser beams in a Nd:YVO4 MOPA system," Chin. Opt. Lett. **15**(12), 120801 (2017).
45. C. Wang, C. Liu, L. Shen, Z. Zhao, B. Liu, and H. Jiang, "16 MW peak power, 90 ps all-solid-state laser from an aberration self-compensated double-passing end-pumped Nd:YVO_4 rod amplifier," Appl. Opt. **55**(9), 2399 (2016).
46. S. Q. Pan, Z. B. Ye, Z. G. Zhao, C. Liu, J. H. Ge, Z. Xiang, and J. Chen, "Beam quality improvement by thermally induced aberrations in a diode-end-pumped laser amplifier," Laser Phys. **23**(9), 095003 (2013).
47. C. Schulze, D. Naidoo, D. Flamm, O. A. Schmidt, A. Forbes, and M. Duparré, "Wavefront reconstruction by modal decomposition," Opt. Express **20**(18), 19714 (2012).
48. W. T. Buono, C. Peters, J. Tau, I. Nape, and A. Forbes, "Eigenmodes of aberrated systems: the tilted lens," J. Opt. **24**(12), 125602 (2022).
49. H. Sroor, C. Moodley, V. Rodríguez-Fajardo, Q. Zhan, and A. Forbes, "Modal description of paraxial structured light propagation: tutorial," J. Opt. Soc. Am. A **38**(10), 1443–1449 (2021).
50. B. P. da Silva, V. Pinillos, D. Tasca, L. Oxman, and A. Khoury, "Pattern revivals from fractional gouy phases in structured light," Phys. Rev. Lett. **124**(3), 033902 (2020).
51. R.-Y. Zhong, Z.-H. Zhu, H.-J. Wu, C. Rosales-Guzmán, S.-W. Song, and B.-S. Shi, "Gouy-phase-mediated propagation variations and revivals of transverse structure in vectorially structured light," Phys. Rev. A **103**(5), 053520 (2021).